


 Cite this: *RSC Adv.*, 2022, **12**, 20946

Synergistic effect of photocatalysis and peroxyomonosulfate activated by MFe_2O_4 ($M = Co, Mn, or Zn$) for enhanced photocatalytic activity under visible light irradiation[†]

 Mingyang Long,^a Di Li,^{id} *a Hongmiao Li,^a Xinguo Ma,^{id} ^c Qianqian Zhao,^a Qi Wen^a and Fang Song^b

Nanosized MFe_2O_4 ($M = Co, Mn, or Zn$) photocatalysts were synthesized *via* a simple sol–gel method. MFe_2O_4 photocatalysts exhibited lower photocatalytic activity for the degradation of levofloxacin hydrochloride under visible light irradiation. For enhancement of photocatalytic activity, MFe_2O_4 was used to activate peroxyomonosulfate and degrade levofloxacin hydrochloride under visible light irradiation. The influences of peroxyomonosulfate dosage, levofloxacin hydrochloride concentration, pH value, and temperature on peroxyomonosulfate activation to degrade levofloxacin hydrochloride were investigated in detail. The mechanism of activation of peroxyomonosulfate by MFe_2O_4 was proposed and proved by radical quenching experiments, electron spin resonance analysis, X-ray photoelectron spectroscopy, electrochemical impedance spectroscopy, and transient photocurrent responses. The combined activation effects of photogenerated e^-/h^+ and transition metals on peroxyomonosulfate to produce sulfate radical clearly enhanced the degradation efficiency.

Received 8th June 2022

Accepted 9th July 2022

DOI: 10.1039/d2ra03558h

rsc.li/rsc-advances

1 Introduction

With the rapid development of aquaculture, antibiotics are widely used to treat infectious diseases of fish. However, remnant antibiotic drugs have the potential to harm people and the environment.^{1,2} Levofloxacin hydrochloride is a quinolone with antibacterial activities.^{3,4} Residual levofloxacin hydrochloride in water can increase the resistance of microbes, which is harmful to human health and safety.^{5–7} Hence, it is important to develop a method to remove the levofloxacin hydrochloride in water.

Photocatalytic technology is an advanced oxidation method that is an outstanding achievement for water treatment because it is inexpensive and produces no secondary pollution.^{8,9} The photocatalytic reaction produces free radicals in a chain reaction until the end products of degradation are CO_2 and H_2O . For wastewater treatment, there is higher research value in the photocatalytic reaction for the treatment of pollutants because of its low selectivity, rapid reaction process, and simple operation compared with conventional oxidation technology.¹⁰

Fe-based heterogeneous catalysts have been widely explored and studied because they are environmentally friendly, inexpensive, and non-toxic compared to other metals. In addition, spinel ferrite nanoparticles are magnetic semiconductors and have been used for activating peroxyomonosulfate (PMS).^{11–13} Ferrite nanoparticles are a magnetic nanomaterial that can be simply recycled from solution by applying an external magnetic field. The presence of ferrite magnetic nanoparticles greatly increases the efficiency of pollutant removal. These materials directly activate PMS to produce sulfate radical (SO_4^{2-}). Previous conductivity measurements determined that the band gaps of $CoFe_2O_4$, $MnFe_2O_4$, and $ZnFe_2O_4$ were in the range of 0.5–0.6 eV.^{14–16} This indicates that $CoFe_2O_4$, $MnFe_2O_4$, and $ZnFe_2O_4$ can be considered as narrow band gap semiconductors that can absorb a greater amount of visible light, and their narrow band gaps allow sunlight to be fully utilized. Furthermore, $CoFe_2O_4$, $MnFe_2O_4$, and $ZnFe_2O_4$ nanoparticles increase the efficiency of removal and can be simply recycled from a heterogeneous suspension using an external magnetic field after the completion of photocatalytic reactions. Thus, secondary pollution created by the disposal of photocatalysts would not be produced.^{17–20}

In this work, nanosized MFe_2O_4 ($M = Co, Mn, or Zn$) photocatalysts were synthesized by a sol–gel method. To further increase the degradation efficiency of levofloxacin hydrochloride, MFe_2O_4 photocatalysts were used to activate PMS under visible light irradiation. In addition to photogenerated e^-/h^+ ,

^aSchool of Chemistry and Chemical Engineering, Xi'an University of Architecture and Technology, Xi'an, 710055, China. E-mail: di.li@xauat.edu.cn

^bInstrument Analysis Center, Xi'an University of Architecture and Technology, Xi'an, 710055, China

^cSchool of Science, Hubei University of Technology, Wuhan 430068, China

† Electronic supplementary information (ESI) available. See <https://doi.org/10.1039/d2ra03558h>



Fe, Co, Mn, and Zn can also activate PMS to produce SO_4^{2-} , and thus, the combined activation effects of photogenerated e^-/h^+ and transition metals on PMS to produce SO_4^{2-} can clearly enhance the degradation efficiency. The influences of PMS dosage, pH value, levofloxacin hydrochloride concentration, and temperature on PMS activation were investigated in detail. Moreover, the degradation mechanisms used by MFe_2O_4 photocatalysts to activate PMS were systematically studied.

2 Experimental

2.1 Materials

Levofloxacin hydrochloride (LVX) of analytical reagent grade quality was used without further purification. Potassium peroxymonosulfate ($2\text{KHSO}_5 \cdot 3\text{KHSO}_4 \cdot \text{K}_2\text{SO}_4$, Oxone®) (PMS) was purchased from Sigma-Aldrich. Other chemicals were analytical or reagent grade commercial products. All solutions were prepared with deionized water.

2.2 Preparation of MFe_2O_3

First, 4 mmol $\text{Fe}(\text{NO}_3)_3 \cdot 9\text{H}_2\text{O}$, 2 mmol $\text{Co}(\text{NO}_3)_2 \cdot 6\text{H}_2\text{O}$, and 12 mmol citric acid were dissolved in a mixture of deionized water (10 mL) and ethanol (20 mL), which was maintained at 70 °C until it entered into the gel state. The gel was dried at 80 °C until it formed a xerogel, which was calcined in a muffle furnace at 550 °C for 5 hours with a heating rate of 5 °C min⁻¹ to obtain CoFe_2O_4 powder. The ZnFe_2O_4 sample was prepared using the same protocol. However, the MnFe_2O_4 sample was calcined at 400 °C for 5 hours, although the other preparation steps were carried out in the same manner as those for CoFe_2O_4 .

2.3 Characterizations

The UV-Vis diffuse reflectance spectra (UV-Vis DRS) of the samples were obtained on a UV-Vis spectrophotometer (Lambda 950, PerkinElmer) using an integrating sphere accessory, and BaSO_4 was used as a reflectance standard. X-ray diffraction (XRD) experiments were carried out using a Rigaku D/MAX 2500 diffractometer with $\text{Cu K}\alpha$ radiation. The size and morphologies of MFe_2O_4 were characterized with the aid of a JSM-7000F field emission scanning electron microscope. Fourier transform infrared (FT-IR) spectroscopy was recorded on a Thermo Nicolet iS5 spectrometer with a KBr disk. The magnetic property was measured at room temperature with the Quantum Design MPMS-SQUID VSM-094. X-ray photoelectron spectroscopy (XPS) measurements were performed using a Kratos AXIS ULTRA DLD. Electron paramagnetic resonance (EPR) measurements of spin-trapped radicals with spin-trap reagent 5,5-dimethyl-1-pirroline-N-oxide (DMPO) (Sigma-Aldrich) were carried out at room temperature with a Bruker A300 spectrometer equipped with a high-pressure mercury lamp as the irradiation source. To minimize experimental errors, the same type of quartz capillary tube was used for all EPR measurements. An EPR spectrometer was coupled to a computer for data acquisition and instrument control.

2.4 Photo-electrochemical properties

Photo-electrochemical measurements were carried out using a conventional three-electrode, single-compartment glass cell fitted with a synthesized quartz window using a potentiostat. The quartz electrolytic cell was filled with 0.1 M Na_2SO_4 . A total of 10 mg of synthesized MFe_2O_4 was dropped onto the ITO glass (2.0 × 4.0 cm), which was used as a working electrode for electrochemical impedance spectroscopy (EIS) and chronoamperometry experiments. A 500 W xenon lamp (Institute of Electric Light Source, Beijing) was used as the light source for the visible light irradiation in the photoelectrochemical analyses. A 420 nm cutoff filter was placed onto the window face of the cell to ensure the desired irradiation conditions. The counter and reference electrodes were a platinum black wire and Ag/AgCl electrode, respectively. The photoelectrochemical experiment was performed using an electrochemical system (Shanghai Chenhua-CHI660e).

2.5 Photocatalytic oxidative degradation

The photocatalytic activities of MFe_2O_4 were evaluated by LVX decomposition under visible light irradiation. In the case of visible light irradiation, a 300 W halogen lamp (Philips Plusline, Shanghai) was focused through a window. A 420 nm cutoff filter was placed onto the window face of the cell to ensure the desired irradiation conditions. The average light intensity was 65 mW cm⁻². The radiant flux was measured with a power meter (Beijing Normal University, Beijing).

A cylindrical double-layer glass photochemical reactor with internal diameter 70 mm, external diameter 80 mm, and height 100 mm was utilized for the photocatalysis reaction. A distance of approximately 17 cm between the lamp and reactor was maintained. Running water was piped into the layer to maintain a constant temperature.

The photocatalytic degradation of LVX in aqueous solution was studied using MFe_2O_4 as the photocatalyst at room temperature and under normal atmospheric pressure. MFe_2O_4 (50 mg) and 100 mL LVX (10 mg L⁻¹) aqueous solution were added to the reactor, and then stirred with a magnetic stirrer prior to irradiation by a halogen lamp at room temperature. Prior to irradiation, the solution was incubated in the dark for 30 min to ensure equilibrium of the working solution. After the reaction, the sample solution was centrifuged to remove MFe_2O_4 , and the solution obtained this way was extracted into a quartz cell. The absorbance of the samples was measured using quartz cells every 10 min.

For the photocatalytic test of MFe_2O_4 activating PMS, MFe_2O_4 was dispersed into LVX solution and magnetically stirred in the dark for 30 min to ensure adsorption–desorption equilibrium. A certain amount of PMS was added to the reactor, and the concentration of LVX solution was monitored by measuring the absorbance as the initial concentration as C_0 . Then, the lamp was turned on to initiate the photodegradation reaction. After five min, 3 mL of the solution was removed and filtered using a 0.22 mm membrane to separate the catalyst powders from the solution, where the instantaneous concentration of LVX was measured every 10 min as C .



3 Results and discussion

3.1 Controlling the synthesis of MFe_2O_4

The XRD patterns were used to study the crystal structure of MFe_2O_4 . The XRD patterns of the phase characteristics and crystalline structure information for MFe_2O_4 are shown in Fig. 1. For CoFe_2O_4 nanoparticles, the diffraction peaks of all the samples were easily indexed as CoFe_2O_4 , which were in agreement with the standard card (JCPDS card number: 79-1744, $R\bar{3}m$ (166) Space Group) with major peaks at $2\theta = 18.28^\circ$, 30.08° , 35.43° , 37.06° , 43.05° , 56.04° , and 62.52° corresponding to the diffractions of (003), (104), (113), (006), (024), (125), and (119), respectively. For MnFe_2O_4 , the diffraction peaks of all the samples were easily indexed as MnFe_2O_4 , which were in agreement with the standard card (JCPDS card number: 73-1964, $Fd\bar{3}m$ (227) Space Group) with major peaks at $2\theta = 18.03^\circ$, 29.66° , 34.93° , 42.44° , 56.10° , and 61.59° corresponding to (111), (220), (311), (400), (333), and (440), respectively. For ZnFe_2O_4 , the diffraction peaks of all the samples were easily indexed as ZnFe_2O_4 , which were in agreement with the standard card (JCPDS card number: 73-1963, $Fd\bar{3}m$ (227) Space Group) with major peaks at $2\theta = 18.38^\circ$, 30.24° , 35.63° , 43.30° , 57.28° , and 62.91° corresponding to (111), (220), (311), (400), (511), and (440), respectively.

The microstructures of MFe_2O_4 were observed by scanning electron microscopy (SEM), as shown in Fig. 2a-d. The CoFe_2O_4 , MnFe_2O_4 , and ZnFe_2O_4 nanoparticles were agglomerated together. The CoFe_2O_4 result (Fig. 2a and b) shows agglomerated nanoparticles 10–20 nm in size. The MnFe_2O_4 (Fig. 2c) particle size was approximately 30 nm, and the ZnFe_2O_4 nanoparticles (Fig. 2d) were 20–30 nm in size.

3.2 FT-IR spectrum and the optical properties of MFe_2O_4

The FT-IR spectrum of MFe_2O_4 is shown in Fig. 3. For CoFe_2O_4 , the absorption band at 1113 cm^{-1} is characteristic of the cobalt ferrite system, and this may be due to the residual FeOOH . The absorption bands present at approximately 568 cm^{-1} were due to the stretching vibrations of metal oxide in the octahedral group complex $\text{Co}(\text{II})-\text{O}^{2-}$ and $\text{Fe}(\text{III})-\text{O}^{2-}$ tetrahedral group complex of the cobalt ferrite phase, respectively, which proves the existence of spinel ferrite.²¹ The peaks at 1635 cm^{-1} , 2336 cm^{-1} , and 3373 cm^{-1} were attributed to the vibrational stretching of the $\text{O}-\text{H}$ bond of H_2O due to the bending of the

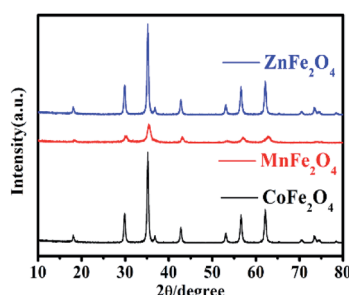


Fig. 1 The XRD pattern of MFe_2O_4 prepared by a sol–gel method.

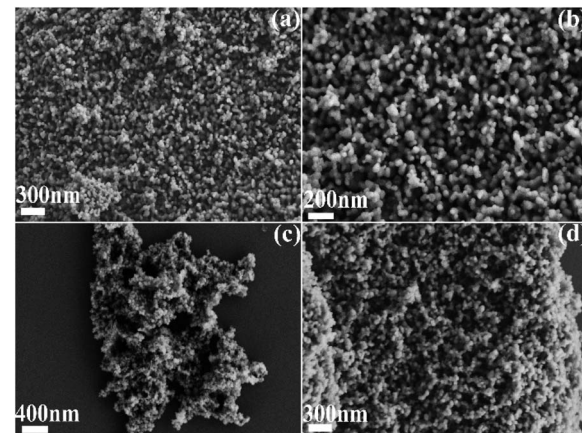


Fig. 2 SEM images of MFe_2O_4 : (a) CoFe_2O_4 , (b) CoFe_2O_4 , (c) MnFe_2O_4 , and (d) ZnFe_2O_4 .

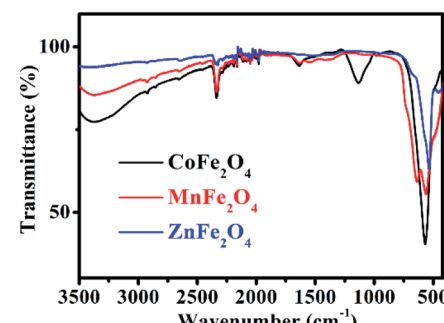


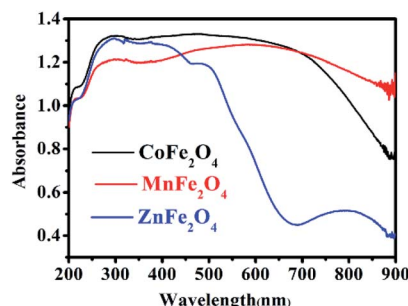
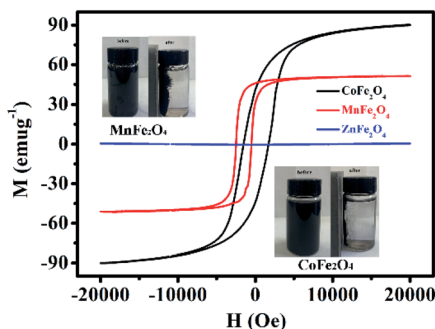
Fig. 3 FT-IR spectra of MFe_2O_4 .

absorbed water molecules.²² For MnFe_2O_4 , the characteristic peaks at approximately 563 cm^{-1} and 637 cm^{-1} corresponded to the formation of Mn–O and Fe–O bonds at the octahedral sites of spinel-type compounds.²³ For ZnFe_2O_4 , the characteristic absorption peaks at 537 cm^{-1} and 452 cm^{-1} denoted the stretching vibration of the Fe–O and Zn–O bonds, indicating the existence of ZnFe_2O_4 .²⁴

UV-Vis diffuse reflectance spectroscopy (DRS) was used to research the optical property of the photocatalysts.²⁵ There was strong absorption for CoFe_2O_4 and MnFe_2O_4 in the range of 200–900 nm, and strong absorption for ZnFe_2O_4 in the range of 200–600 nm, as shown in Fig. 4. Therefore, the visible light was efficiently utilized. The steep shape of the spectra indicated that the visible light absorption was not caused by a transition from the impurity level, but rather, was caused by the band-gap transition.²⁶

3.3 Magnetic properties of MFe_2O_4 photocatalysts

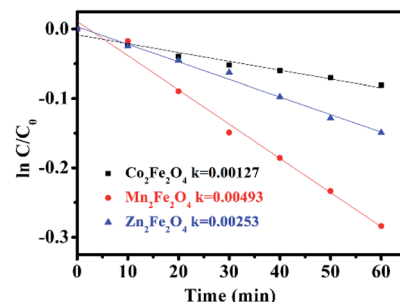
Fig. 5 shows the H–M hysteresis loop of MFe_2O_4 samples prepared by a sol–gel method. There were excellent magnetic properties for CoFe_2O_4 and MnFe_2O_4 , and the values of specific magnetization (M_s) were 90.8 and 52.3 emu g^{-1} , which thus indicated superparamagnetism. By comparison, ZnFe_2O_4 was 5.02 emu g^{-1} , which was much less than that of CoFe_2O_4 and

Fig. 4 UV-Vis diffuse reflectance spectra of MFe_2O_4 .Fig. 5 Magnetic hysteresis loops of MFe_2O_4 . The inset shows photos of well-dispersed MFe_2O_4 in water and magnetic separation of MFe_2O_4 .

MnFe_2O_4 . Difficulty in recycling of the photocatalyst could significantly hinder its extensive application in wastewater treatment. Thus, by taking advantage of the magnetic properties of CoFe_2O_4 and MnFe_2O_4 , the photocatalysts can be easily recycled for multiple usages. The inset of Fig. 5 shows that CoFe_2O_4 and MnFe_2O_4 can be readily dispersed in water to form a stable solution. In addition, the photocatalyst rapidly responds to the external magnet because of its excellent magnetic properties. After magnetic separation, most of the CoFe_2O_4 and MnFe_2O_4 photocatalyst particles were drawn to the bottle sidewall. As a result, this dispersion and separation process can be repeatedly applied with CoFe_2O_4 and MnFe_2O_4 using an external magnetic field, which is convenient for their reusability in water treatment and minimizes any secondary pollution.

3.4 Photocatalytic properties of MFe_2O_4

The photocatalytic activity of MFe_2O_4 was estimated by the removal of LVX. To further depict the photocatalytic reaction, the photocatalytic degradation process was also fitted to pseudo first-order kinetics, and the value of the rate constant k is equal to the corresponding slope of the fitting line, as shown in Fig. 6. The first-order linear relationship was revealed by the plots of $\ln(C/C_0)$ vs. irradiation time (t), where C denotes the concentration of LVX at irradiation time t , and C_0 denotes the concentration during the adsorption equilibrium of the photocatalysts before irradiation. *Via* the first order linear fit, the

Fig. 6 First-order plots for the photocatalytic degradation of LVX using MFe_2O_4 .

determined reaction rate constants k were 0.00269, 0.01003, and 0.00691 min^{-1} , respectively, for CoFe_2O_4 , MnFe_2O_4 , and ZnFe_2O_4 . The strongest photocatalytic activity was exhibited by the MnFe_2O_4 sample.

3.5 Activating PMS with MFe_2O_4 to enhance the degradation efficiency

Recently, there has been increased interest by researchers regarding the advanced oxidation processes (AOPs) of the sulfate radical ($\text{SO}_4^{\cdot-}$).^{27,28} Because of a higher redox potential, the sulfate radical can degrade many organic pollutants.^{29,30} As a monopersulfate compound, PMS can be activated not only by a transition metal, but also by photogenerated e^-/h^+ to generate strong oxidizing sulfate radicals. Therefore, activating PMS to enhance the degradation rate with MFe_2O_4 under visible light irradiation might be a good choice. The degradation rate of LVX in different systems is shown in Fig. 7a–c. The photocatalytic experiments showed that the photocatalytic activity of MFe_2O_4 was low, and its degradation rate was the slowest of all. The degradation rate for the $\text{MFe}_2\text{O}_4/\text{PMS}$ system without visible light was much slower than that of the $\text{MFe}_2\text{O}_4/\text{Vis}/\text{PMS}$ system. The degradation efficiency for activation of PMS with MFe_2O_4 under visible light irradiation was much higher than that for PMS only activated by MFe_2O_4 and MFe_2O_4 only under visible light irradiation. The activation of PMS with MFe_2O_4 resulted from photogenerated e^-/h^+ , Fe, and M, and the degradation rate was much faster than that which occurred when PMS was only activated by MFe_2O_4 .

A comparison between this work and other photocatalyst performances for the degradation of LVX was conducted under the same conditions. As shown in Fig. S1,† the photocatalytic experiments showed that the efficiency of LVX degradation in the $\text{FeWO}_4/\text{Vis}/\text{PMS}$ and $\text{Fe}_2(\text{MoO}_4)_3/\text{Vis}/\text{PMS}$ systems was lower. However, the removal rate increased to 92% in an hour in the $\text{CoFe}_2\text{O}_4/\text{Vis}/\text{PMS}$ system. The removal rate also reached 70–80% in an hour in the $\text{MnFe}_2\text{O}_4/\text{Vis}/\text{PMS}$ and $\text{ZnFe}_2\text{O}_4/\text{Vis}/\text{PMS}$ systems. This indicated that the degradation efficiency for PMS activation with MFe_2O_4 under visible light irradiation was much higher than that with FeWO_4 or $\text{Fe}_2(\text{MoO}_4)_3$.

3.5.1 Effect of PMS dosage, pH value, temperature, and LVX concentration. The effect of PMS dosage on the performance of the $\text{MFe}_2\text{O}_4/\text{Vis}/\text{PMS}$ system towards LVX degradation



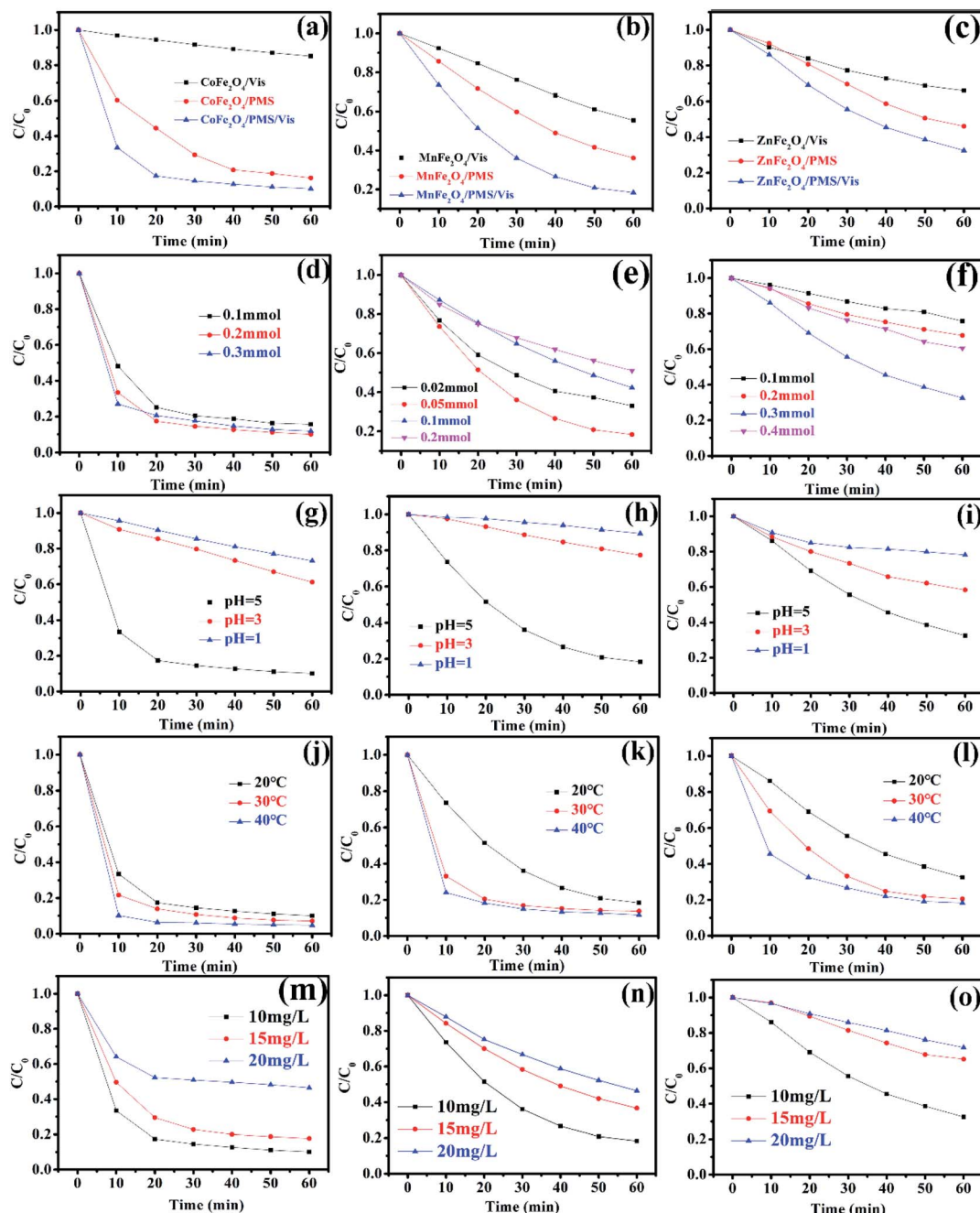
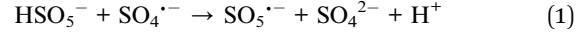


Fig. 7 The degradation rate of MFe_2O_4 in different systems: (a) CoFe_2O_4 , (b) MnFe_2O_4 , (c) ZnFe_2O_4 ([photocatalyst] = 0.5 g L^{-1} , [LVX] = 10 mg L^{-1} , [PMS] = 2 mM , 0.5 mM , and 3 mM for CoFe_2O_4 , MnFe_2O_4 , and ZnFe_2O_4 , respectively); effect of PMS dosages on the degradation of LVX with PMS activated by MFe_2O_4 photocatalysts: (d) CoFe_2O_4 , (e) MnFe_2O_4 , and (f) ZnFe_2O_4 ([photocatalyst] = 0.5 g L^{-1} , [LVX] = 10 mg L^{-1}); effect of pH value on the degradation of LVX: (g) CoFe_2O_4 , (h) MnFe_2O_4 , and (i) ZnFe_2O_4 ([photocatalyst] = 0.5 g L^{-1} , [LVX] = 10 mg L^{-1} , [PMS] = 2 mM , 0.5 mM , and 3 mM for CoFe_2O_4 , MnFe_2O_4 , and ZnFe_2O_4 , respectively); effect of temperature on the degradation of LVX: (j) CoFe_2O_4 , (k) MnFe_2O_4 , and (l) ZnFe_2O_4 ([photocatalyst] = 0.5 g L^{-1} , [LVX] = 10 mg L^{-1} , [PMS] = 2 mM , 0.5 mM , and 3 mM for CoFe_2O_4 , MnFe_2O_4 , and ZnFe_2O_4 , respectively); effect of LVX concentrations on the degradation of LVX: (m) CoFe_2O_4 , (n) MnFe_2O_4 , and (o) ZnFe_2O_4 ([photocatalyst] = 0.5 g L^{-1} , [PMS] = 2 mM , 0.5 mM , and 3 mM for CoFe_2O_4 , MnFe_2O_4 , and ZnFe_2O_4 , respectively).

was investigated (Fig. 7d-f). The LVX degradation rate increased with the increase in the PMS dosage in all systems, and thus, the more dosages of PMS that were added, the more SO_4^{2-} that was produced. However, the degradation rate gradually decreased when the PMS dosage continuously increased, which was

ascribed to the self-quenching effect between the sulfate radicals and PMS (eqn (1)).^{31,32} The experimental results indicated that the optimal dosage of PMS was 0.2 mmol , 0.05 mmol , and 0.3 mmol , respectively, for CoFe_2O_4 , MnFe_2O_4 , and ZnFe_2O_4 .



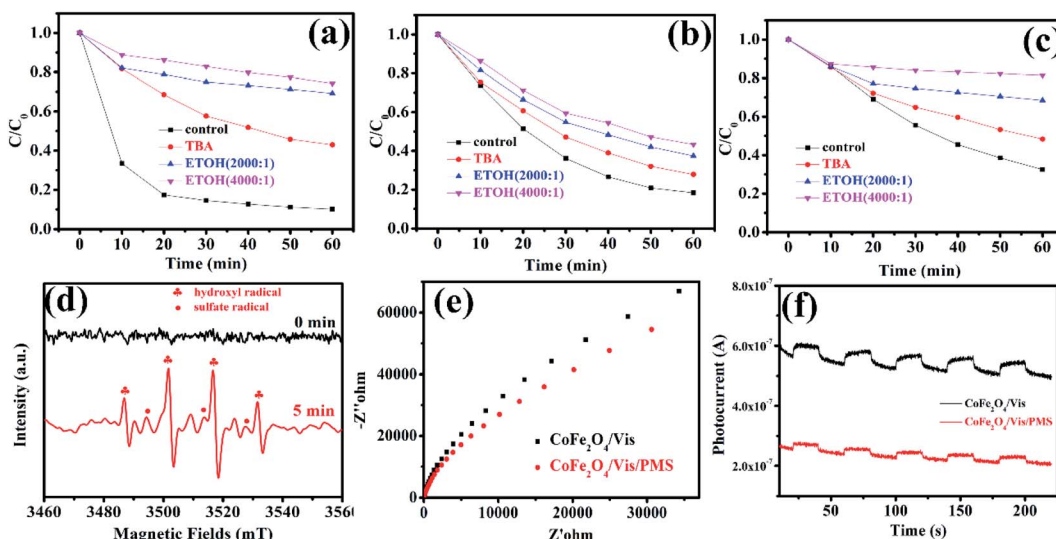


Fig. 8 Effects of tert-butyl alcohol and ethanol addition on the photocatalytic degradation of LVX ([photocatalyst] = 0.5 g L⁻¹, [LVX] = 10 mg L⁻¹, [PMS] = 2 mM, 0.5 mM, and 3 mM for CoFe₂O₄, MnFe₂O₄, and ZnFe₂O₄, respectively): (a) CoFe₂O₄, (b) MnFe₂O₄, (c) ZnFe₂O₄; (d) EPR spectra of CoFe₂O₄ under visible light irradiation (DMPO as the radical trapper); (e) electrochemical impedance spectroscopy of CoFe₂O₄ sample electrodes with and without PMS under visible light irradiation ($\lambda > 420$ nm); (f) transient photocurrent responses of CoFe₂O₄ sample electrodes with and without PMS under visible light irradiation ($\lambda > 420$ nm).

The pH value had an obvious effect on PMS activation, which was confirmed by a previous study.³³ Therefore, the effect of the pH value on the degradation rate was studied. As exhibited in Fig. 7g-i, the results showed that the pH value clearly influenced the degradation efficiency. According to published literature, it was mainly attributed to the fact that H⁺ hindered the production of OH[·] and SO₄²⁻, resulting in a decrease in the number of active radicals.³⁴ Therefore, the removal rate increased as the pH value increased.

The influence of the initial temperature on the removal of LVX by the MFe₂O₄ photocatalyst was further investigated. As shown in Fig. 7j-l, the degradation rate increased with increasing temperature, which was due to PMS activation in the endothermic reaction and a higher reactive oxygen species (ROS) production rate at higher temperatures, with LVX being degraded by CoFe₂O₄ in 10 min at 40 °C. This might be caused by the self-activation reaction of PMS under higher temperatures.³²

The effects of initial LVX concentration on the degradation behaviour are shown in Fig. 7m-o. As the initial levofloxacin concentration increased from 10 mg L⁻¹ to 20 mg L⁻¹, the degradation kinetics decreased. This may have occurred due to the higher concentration of LVX that resulted in additional active ROS being produced.³² However, the limited photocatalysts and PMS could not produce sufficient radicals to degrade a solution with higher LVX concentration.

3.5.2 Degradation mechanism after PMS activation with MFe₂O₄. To investigate the degradation mechanism that occurs after activation of PMS with MFe₂O₄ and confirm the role of the active species in the degradation process, *tert*-butanol and ethanol were introduced as radical scavengers. Ethanol was chosen as the radical scavenger for the sulfate radical and hydroxyl radical.³² However, *tert*-butanol was the only effective scavenger for the hydroxyl radical.³⁵⁻³⁷ After 1 mmol *tert*-butanol

was added to LVX solution, there was not an obvious inhibitory effect (Fig. 8a-c), which indicated that the hydroxyl radical was not the primary active specie in the MFe₂O₄/PMS/Vis system. Obvious inhibition of the degradation rate was observed after excess ethanol was added to the LVX solution, in which the molar ratio of ethanol and PMS was 2000 : 1 (Fig. 8a-c). When the molar ratio was increased to 4000 : 1, the inhibition of the degradation rate was more obvious, which indicated that sulfate radical was the key active specie in the Vis/MFe₂O₄/PMS system.

To confirm the above results, electron paramagnetic resonance (EPR) spectroscopy was used to trace intermediate radical species that existed in the Vis/CoFe₂O₄/PMS system. The trapping agent 5,5-dimethylpyrrolineoxide (DMPO) was used to capture radicals ·OH and SO₅²⁻ in the Vis/CoFe₂O₄/PMS system.^{38,39} As shown in Fig. 8d, the characteristic peak signals of DMPO-·OH and DMPO-SO₅²⁻ adducts were found,⁴⁰ which not only proved the coexistence of ·OH and SO₄²⁻ species, but also supported the sole activity of SO₄²⁻ in this system.

Electrochemical impedance spectroscopy (EIS) was used to characterize electrochemical interfacial reactions. The photocatalytic decomposition of LVX can be explained as an electrochemical oxidation reaction in which reactants supply electrons to an anode. A smaller arc radius of the EIS Nyquist plot represents a faster electron transfer rate and a more efficient electron-hole separation.⁴¹ Fig. 8e shows the EIS response of CoFe₂O₄ under visible light irradiation ($\lambda > 420$ nm). The radius of the arc on the EIS Nyquist plot reflects the reaction rate occurring at the surface of the electrode. The radii tended to significantly decrease after adding PMS to the solution, indicating that both charge-transfer resistance and capacitive reactance decreased. This suggested that there was an effective separation of photogenerated electron-hole pairs and that fast interfacial charge transfer to the electron donor/electron

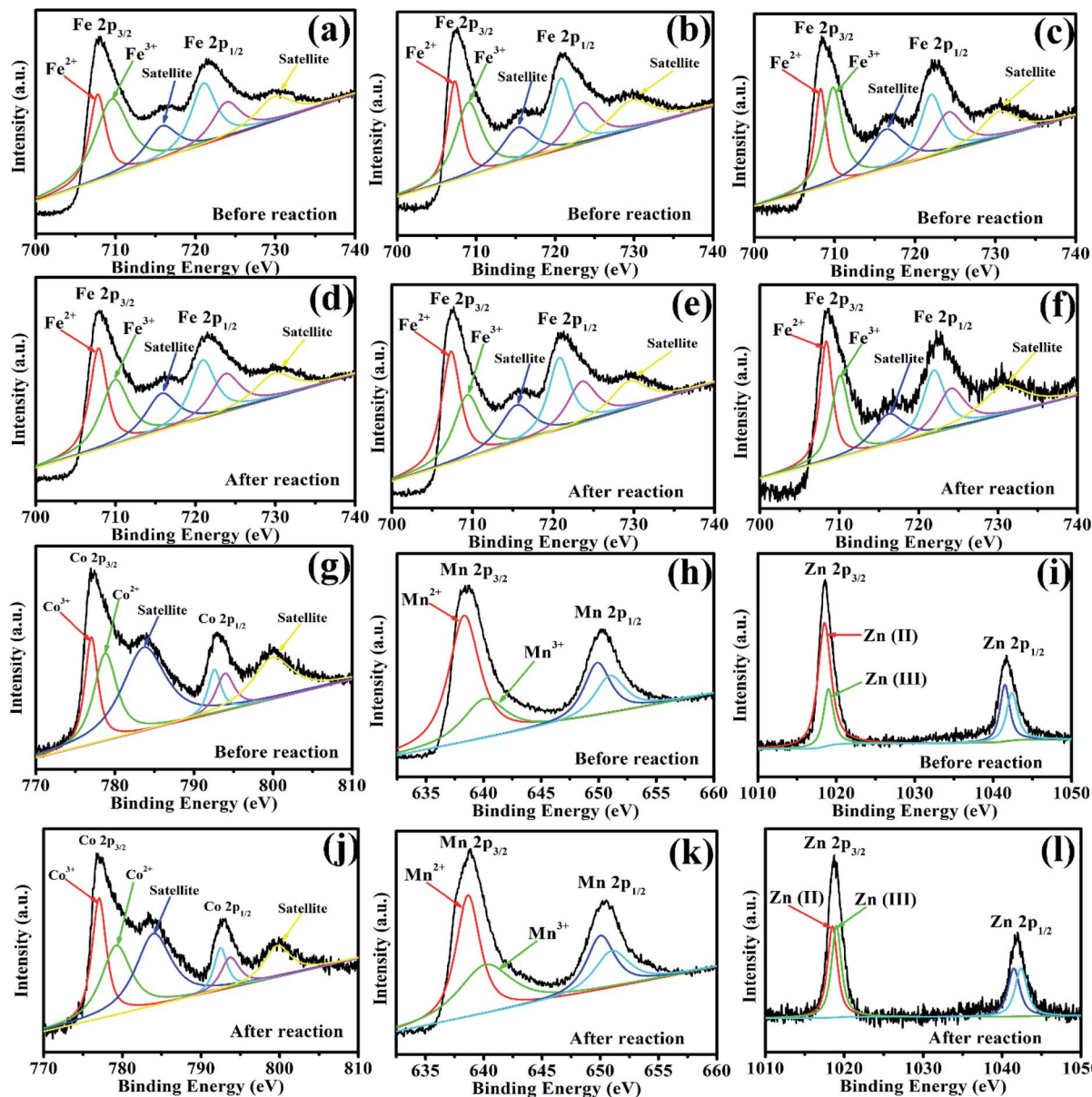


Fig. 9 (a, d, g, and j) XPS spectra of Fe 2p and Co 2p for CoFe_2O_4 before and after photocatalytic oxidation of LVX. (b, e, h, and k) XPS spectra of Fe 2p and Mn 2p for MnFe_2O_4 before and after photocatalytic oxidation of LVX. (c, f, i, and l) XPS spectra of Fe 2p and Zn 2p for ZnFe_2O_4 before and after photocatalytic oxidation of LVX.

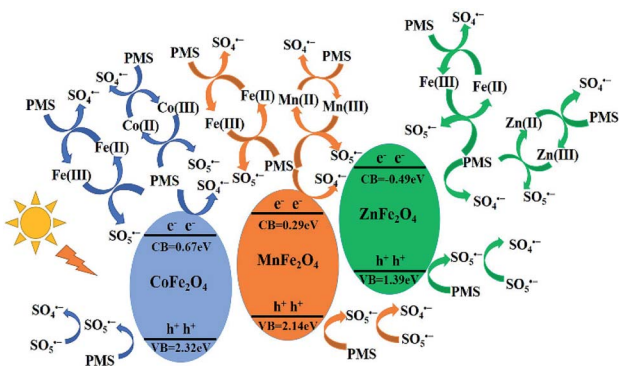
acceptor occurred, as suggested by Leng *et al.*⁴² With the existence of PMS, the interfacial electron transfer rate and the electron–hole separation efficiency of the Vis/ CoFe_2O_4 /PMS system greatly increased.

To further confirm that PMS efficiently captured the photo-generated electrons in the Vis/ CoFe_2O_4 /PMS system, the transient photocurrent responses of CoFe_2O_4 were also measured under visible light irradiation. As shown in Fig. 8f, the introduction of PMS significantly decreased the density of photocurrent in the Vis/ CoFe_2O_4 /PMS system. It is likely that the photogenerated electrons were efficiently trapped by the PMS, which was consistent with results from a previous report.⁴³

To investigate the role of iron, zinc, and manganese in Vis/ MnFe_2O_4 /PMS systems, the XPS spectrum was used to analyze the

samples before and after photocatalytic experiments (Fig. 9). In the XPS spectrum of CoFe_2O_4 , the Fe 2p peaks at 707.95 eV and 721.53 eV were assigned to $\text{Fe} 2\text{p}_{3/2}$ and $\text{Fe} 2\text{p}_{1/2}$ (Fig. 9a and d), respectively, showing that a portion of Fe species existed in the form of Fe^{2+} in CoFe_2O_4 before the photocatalytic experiment. However, the area of Fe^{3+} peaks decreased, and the area of Fe^{2+} peaks increased after activation of PMS with CoFe_2O_4 , which indicated that Fe^{3+} on the surface of CoFe_2O_4 was partially transformed to Fe^{2+} .⁴⁴ This proved that the regeneration of $\text{Fe}(\text{III})$ and a cycle of $\text{Fe}(\text{III})/\text{Fe}(\text{II})$ occurred in the Vis/ CoFe_2O_4 /PMS systems.⁴⁵ The Co 2p peaks at 776.93/45 and 792.98 eV were assigned to the binding energies of $\text{Co} 2\text{p}_{3/2}$ and $\text{Co} 2\text{p}_{1/2}$ (Fig. 9g and j), respectively, indicating that a portion of Co species existed in the form of Co^{3+} . However, the area of the

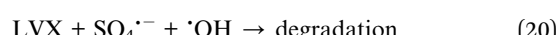
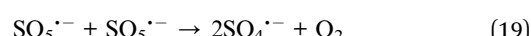
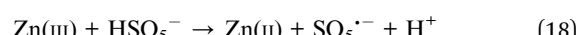
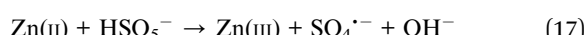
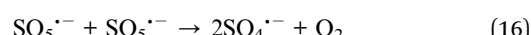
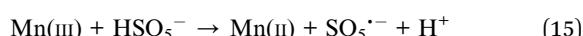
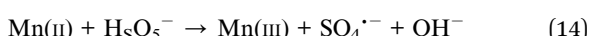
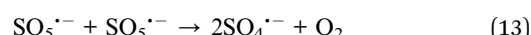
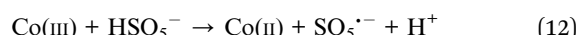
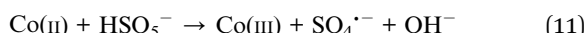
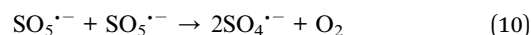
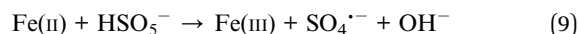
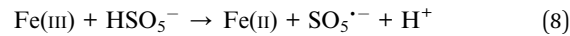
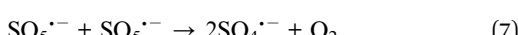
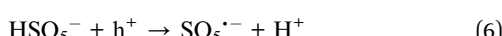
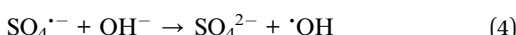
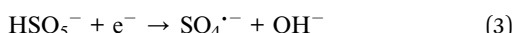
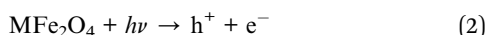




Scheme 1 Schematic drawing illustrating the mechanism of activation of PMS with MFe_2O_4 photocatalyst under visible light irradiation.

Co^{2+} peaks decreased, and the area of the Co^{3+} peaks increased after activation of PMS with CoFe_2O_4 , which indicated that Co^{2+} on the surface of CoFe_2O_4 was partially transformed to Co^{3+} .⁴⁵ This proved that regeneration of $\text{Co}(\text{II})$ and a cycle of $\text{Co}(\text{II})/\text{Co}(\text{III})$ occurred in the Vis/ CoFe_2O_4 /PMS systems. Similar conclusions were drawn from the XPS spectra (Fig. 9) of MnFe_2O_4 and ZnFe_2O_4 before and after activation of PMS. It proved that cycles of $\text{Fe}(\text{III})/\text{Fe}(\text{II})$, $\text{Co}(\text{II})/\text{Co}(\text{III})$, $\text{Mn}(\text{II})/\text{Mn}(\text{III})$, and $\text{Zn}(\text{II})/\text{Zn}(\text{III})$ existed in the Vis/ MFe_2O_4 /PMS systems.

According to the above results, the mechanism of activating PMS with MFe_2O_4 is shown in Scheme 1 (eqn (2)–(20)). The MFe_2O_4 photocatalyst absorbed visible light and then produced photogenerated e^-/h^+ pairs.⁴⁶ PMS was activated by photogenerated electrons (e^-) and then produced $\text{SO}_4^{•-}$ radicals. $\text{SO}_4^{•-}$ reacted with OH^- to form OH^\bullet and SO_4^{2-} . SO_4^{2-} then reacted with h^+ to form $\text{SO}_4^{•-}$. The h^+ also activated PMS to produce $\text{SO}_5^{•-}$, and then, $\text{SO}_5^{•-}$ reacted with each other to generate $\text{SO}_4^{•-}$ (eqn (2)–(7)).^{47,48} PMS was also activated by iron to produce sulfate radicals. Because of the effective electron transfer from PMS to $\text{Fe}(\text{III})$ and $\text{Fe}(\text{II})$, which resulted in regeneration of $\text{Fe}(\text{III})$ and cycling between $\text{Fe}(\text{III})$ and $\text{Fe}(\text{II})$, enhanced degradation efficiency was achieved in activating PMS with CoFe_2O_4 under visible light irradiation (eqn (8)–(10)).⁴⁴ Similarly, there was also regeneration of $\text{Co}(\text{II})$ and cycling between $\text{Co}(\text{II})$ and $\text{Co}(\text{III})$ for CoFe_2O_4 (eqn (11)–(13)),⁴⁵ which indicated that cobalt also activates PMS to enhance the degradation efficiency, in addition to iron. MnFe_2O_4 and ZnFe_2O_4 activated PMS and regenerated in the same manner as that of CoFe_2O_4 (eqn (14)–(19)).⁴⁴ Finally, LVX was mainly degraded by sulfate radicals and hydroxyl radicals (eqn (20)).^{49–51}

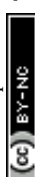


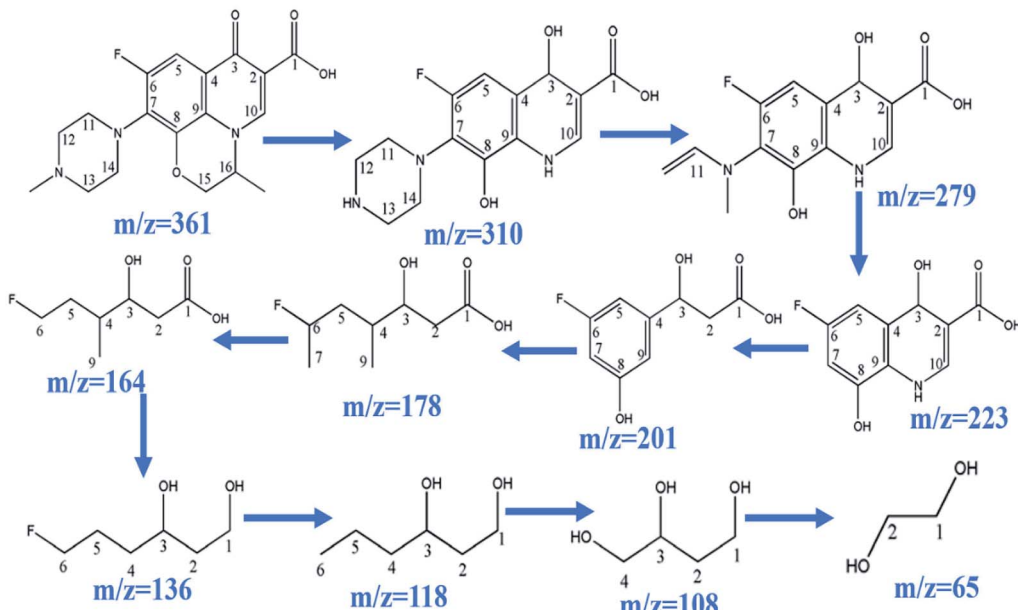
3.6 The degradation pathway of LVX

During the process of CoFe_2O_4 activating PMS to enhance degradation efficiency under visible light irradiation, the $\text{SO}_4^{•-}$ attacks LVX and then disassembles its molecular structure. The intermediate products then form, and the possible degradation pathways are shown in Scheme 2 by UPLC-MS analysis (Fig. S2†). As the weak electron donor, methyl groups facilitate the attack on LVX by electrophilic species ($\text{SO}_4^{•-}$) in the demethylation process, resulting in the formation of the intermediate product of $m/z = 310$. With sustained degradation, the $\text{SO}_4^{•-}$ cleaved the ring, and the intermediate products of $m/z = 279$ were formed.⁵² With photodegradation proceeding, the nitrogen bonded with C7 was exfoliated to obtain the compound of $m/z = 223$. Then, the $\text{SO}_4^{•-}$ continued to attack the intermediate products and disconnect the ring of the intermediate structure, and the intermediate compound of $m/z = 178$ formed. As photodegradation proceeded, $\text{SO}_4^{•-}$ continued to cleave the functional groups, and glycol was formed ($m/z = 65$). Finally, the above intermediate products were mineralized into H_2O , CO_2 , and others.

3.7 Stability of MFe_2O_4

To study the reusability and stability of photocatalysts, recycling experiments were carried out (Fig. S3a–c†). When the degradation experiment was finished, the CoFe_2O_4 was filtered from the LVX solution. The CoFe_2O_4 was further dried at 60 °C and was used for the next degradation experiment. After three recycling experiments, there were no obvious changes in LVX degradation. Similarly, recycling experiments were conducted in Vis/ MnFe_2O_4 /PMS and Vis/ ZnFe_2O_4 /PMS systems. It was found that





Scheme 2 Possible degradation pathway of LVX.

there was satisfactory reusability and stability for the three photocatalysts.

4 Conclusions

Nanosized MFe_2O_4 was successfully synthesized by a simple sol-gel method. The photocatalytic properties of MFe_2O_4 were investigated under visible light irradiation, and they showed decreased photocatalytic activity for the degradation of levofloxacin hydrochloride under visible light irradiation. For enhanced photocatalytic activity, MFe_2O_4 was used to activate peroxymonosulfate to degrade levofloxacin hydrochloride under visible light irradiation. A series of systematic experiments proved that the PMS dosage conferred an obvious effect on the degradation rate. Furthermore, there was a noteworthy effect by the levofloxacin hydrochloride concentration and the pH value on the levofloxacin hydrochloride degradation. After activation of PMS with MFe_2O_4 , a degradation mechanism was proposed and proved by EPR, EIS, transient photocurrent, and XPS. Kinetic studies using radical scavenger technologies suggested that sulfate radical controls the degradation process.

Author contributions

Di Li: project administration, Mingyang Long: investigation, Hongmiao Li: data curation, Xinguo Ma: methodology, Qian-qian Zhao: formal analysis, and Qi Wen: writing – review and editing.

Conflicts of interest

There are no conflicts to declare.

Acknowledgements

This work was supported by the National Natural Science Foundation of China (21301135) and Xi'an University of Architecture and Technology Science Foundation (ZR21068). We thank Ms Fang Song at the Instrument Analysis Center of Xi'an University of Architecture and Technology for her assistance with the SEM analysis, and also thank Eceshi (<https://www.eceshi.com>) for the EPR and photo-electrochemical measurements.

Notes and references

- 1 F. Wang, Z. Chen, Z. Zhu and J. Guo, *J. Mater. Res. Technol.*, 2022, **17**, 1696–1706.
- 2 S. Liu, X. Jiang, G. I. N. Waterhouse, Z.-M. Zhang and L.-m. Yu, *Sep. Purif. Technol.*, 2022, **294**, 121094.
- 3 S. Altaf, R. Zafar, W. Q. Zaman, S. Ahmad, K. Yaqoob, A. Syed, A. J. Khan, M. Bilal and M. Arshad, *Ecotoxicol. Environ. Saf.*, 2021, **226**, 112826.
- 4 J. Xu, M. Zhang, X. Li and M. Chen, *J. Environ. Chem. Eng.*, 2022, **10**, 107484.
- 5 M. R. Abukhadra, A. A. AlHammadi, J. Seong Khim, J. S. Ajarem and A. A. Allam, *J. Cleaner Prod.*, 2022, **356**, 131836.
- 6 J. Liang, Y. Hou, H. Zhu, J. Xiong, W. Huang, Z. Yu and S. Wang, *Chem. Eng. J.*, 2022, **433**, 133574.
- 7 L. A. Goulart, A. Moratalla, P. Cañizares, M. R. V. Lanza, C. Sáez and M. A. Rodrigo, *J. Environ. Chem. Eng.*, 2022, **10**, 107317.
- 8 R. Nawaz, C. F. Kait, H. Y. Chia, M. H. Isa, L. W. Huei, N. T. Sahrin and N. Khan, *Environ. Technol. Innovation*, 2021, **23**, 101764.



9 Y.-W. Li and W.-L. Ma, *Chemosphere*, 2021, **280**, 130667.

10 S. Jian, Z. Tian, J. Hu, K. Zhang, L. Zhang, G. Duan, W. Yang and S. Jiang, *Adv. Powder Technol. Mater.*, 2022, **1**, 100004.

11 Y. Yao, Y. Cai, F. Lu, F. Wei, X. Wang and S. Wang, *J. Hazard. Mater.*, 2014, **270**, 61–70.

12 A. Manohar, V. Vijayakanth, S. V. P. Vattikuti and K. H. Kim, *Mater. Chem. Phys.*, 2022, **286**, 126117.

13 Y. Lu, M. Yousaf, M. N. Akhtar, A. Noor, M. Akbar, M. A. K. Y. Shah, S. Yan and F. Wang, *Ceram. Int.*, 2022, **48**, 2782–2792.

14 H. D. Abdul kader, I. S. Mohammed and S. H. Ammar, *Environ. Nanotechnol. Monit. Manage.*, 2022, **17**, 100664.

15 H. B. Desai, L. J. Hathiya, H. H. Joshi and A. R. Tanna, *Mater. Today: Proc.*, 2020, **21**, 1905–1910.

16 M. M. Sabzehei, H. Karimi, M. Ghaedi and V. M. Avargani, *Mater. Res. Bull.*, 2021, **143**, 111449.

17 J. Wang, J. Li, X. Li, X. Bao and X. Gao, *J. Magn. Magn. Mater.*, 2018, **462**, 53–57.

18 O. Mounkachi, R. Lamouri, E. Salmani, M. Hamedoun, A. Benyoussef and H. Ez-Zahraouy, *J. Magn. Magn. Mater.*, 2021, **533**, 168016.

19 X. Zhang, C. Li, T. Chen, Y. Tan, X. Liu, F. Yuan, S. Zheng and Z. Sun, *Int. J. Min. Sci. Technol.*, 2021, **31**, 1169–1179.

20 Y. Ma, X. Xu, L. Lu, K. Meng, Y. Wu, J. Chen, J. Miao and Y. Jiang, *Ceram. Int.*, 2021, **47**, 34005–34011.

21 M. H. Habibi and H. J. Parhizkar, *Spectrochim. Acta, Part A*, 2014, **127**, 102–106.

22 A. Allabar and M. Nowak, *Chem. Geol.*, 2020, **556**, 119833.

23 N. Akhlaghi and G. Najafpour-Darzi, *J. Mol. Catal.*, 2022, **519**, 112118.

24 C. Akshhayya, M. K. Okla, W. H. Al-Qahtani, M. R. Rajeshwari, A. Mohebaldin, Y. A. Alwasel, W. Soufan, M. A. Abdel-Maksoud, H. AbdElgawad, L. L. Raju, A. M. Thomas and S. S. Khan, *J. Environ. Chem. Eng.*, 2022, **10**, 107673.

25 Y. Ma, J. Du, Y. Fang and X. Wang, *ChemSusChem*, 2021, **14**, 946–951.

26 A. Kudo, I. Tsuji and H. Kato, *Chem. Commun.*, 2002, 1958–1959.

27 W. S. Chen and C. P. Huang, *Chemosphere*, 2015, **125**, 175–181.

28 J. Zou, J. Ma, L. W. Chen, X. C. Li, Y. H. Guan, P. C. Xie and C. Pan, *Environ. Sci. Technol.*, 2013, **47**, 11685–11691.

29 M. M. Ahmed, S. Barbat, P. Doumenq and S. Chiron, *Chem. Eng. J.*, 2012, **197**, 440–447.

30 M. G. Antoniou, A. A. de la Cruz and D. D. Dionysiou, *Environ. Sci. Technol.*, 2010, **44**, 7238–7244.

31 C. Brandt and R. Vaneldik, *Chem. Rev.*, 1995, **95**, 119–190.

32 J. Kang, H. Zhang, X. Duan, H. Sun, X. Tan, S. Liu and S. Wang, *Chem. Eng. J.*, 2019, **362**, 251–261.

33 R. Li, H. Hu, Y. Ma, X. Liu, L. Zhang, S. Zhou, B. Deng, H. Lin and H. Zhang, *J. Cleaner Prod.*, 2020, **276**, 124246.

34 Y. Huang, L. Nengzi, X. Zhang, J. Gou, Y. Gao, G. Zhu, Q. Cheng and X. Cheng, *Chem. Eng. J.*, 2020, **388**, 124274.

35 X. L. Wu, X. G. Gu, S. G. Lu, Z. F. Qiu, Q. Sui, X. K. Zang, Z. W. Miao and M. H. Xu, *Sep. Purif. Technol.*, 2015, **147**, 186–193.

36 G. V. Buxton, C. L. Greenstock, W. P. Helman, A. B. Ross and W. Tsang, *J. Phys. Chem. Ref. Data*, 1988, **17**, 513–886.

37 Y. Liu, H. Guo, Y. Zhang, W. Tang, X. Cheng and H. Liu, *Chem. Phys. Lett.*, 2016, **653**, 101–107.

38 H. Fu, C. Pan, W. Yao and Y. Zhu, *J. Phys. Chem. B*, 2005, **109**, 22432–22439.

39 Y. Wang, L. Zhou, X. Duan, H. Sun, E. L. Tin, W. Jin and S. Wang, *Cataly. Today*, 2015, **258**, 576–584.

40 H. Sun, G. Zhou, Y. Wang, A. Suvorova and S. Wang, *ACS Appl. Mater. Interfaces*, 2014, **6**, 16745–16754.

41 X. Li, X. Chen, Y. Fang, W. Lin, Y. Hou, M. Anpo, X. Fu and X. Wang, *Chem. Sci.*, 2022, **13**, 7541–7551.

42 W. H. Leng, Z. Zhang, J. Q. Zhang and C. N. Cao, *J. Phys. Chem. B*, 2005, **109**, 15008–15023.

43 Y. Gao, Z. Zhang, S. Li, J. Liu, L. Yao, Y. Li and H. Zhang, *Appl. Catal., B*, 2016, **185**, 22–30.

44 C. Tan, N. Gao, D. Fu, J. Deng and L. Deng, *Sep. Purif. Technol.*, 2017, **175**, 47–57.

45 Y. Ren, L. Lin, J. Ma, J. Yang, J. Feng and Z. Fan, *Appl. Catal., B*, 2015, **165**, 572–578.

46 Y. Fang, Y. Hou, X. Fu and X. Wang, *Chem. Rev.*, 2022, **122**, 4204–4256.

47 Z. Shen, H. Zhou, Z. Pan, Y. Guo, Y. Yuan, G. Yao and B. Lai, *J. Hazard. Mater.*, 2020, **400**, 123187.

48 H. Shao, X. Zhao, Y. Wang, R. Mao, Y. Wang, M. Qiao, S. Zhao and Y. Zhu, *Appl. Catal., B*, 2017, **218**, 810–818.

49 H. Huang, T. Guo, K. Wang, Y. Li and G. Zhang, *Sci. Total Environ.*, 2021, **758**, 143957.

50 T. Guo, L. Jiang, K. Wang, Y. Li, H. Huang, X. Wu and G. Zhang, *Appl. Catal., B*, 2021, **286**, 119883.

51 T. Guo, L. Jiang, H. Huang, Y. Li, X. Wu and G. Zhang, *J. Hazard. Mater.*, 2021, **416**, 125838.

52 Z. Zhang, Z. Pan, Y. Guo, P. K. Wong, X. Zhou and R. Bai, *Appl. Catal., B*, 2020, **261**, 118212.

